

# Statistical Evaluation of Mechanical Properties of Thermally Sprayed Alumina Coatings by Nanoindentation Method<sup>\*1</sup>

Kosuke Sanami<sup>1,2</sup>, Kentaro Shinoda<sup>2,\*2</sup>, Atsushi Yumoto<sup>3</sup> and Jun Akedo<sup>4</sup>

<sup>1</sup>Graduate School, Shibaura Institute of Technology, Tokyo 135-8548, Japan

<sup>2</sup>Advanced Coating Technology Research Center, National Institute of Advanced Industrial Science and Technology (AIST), Tsukuba 305-8564, Japan

<sup>3</sup>Shibaura Institute of Technology, Tokyo 135-8548, Japan

<sup>4</sup>Advanced Coating Technology Research Center, National Institute of Advanced Industrial Science and Technology (AIST), Tsukuba 305-8565, Japan

Additional better-quality homogeneous microstructures can be rendered available by the use of finer ceramic particles in thermal spraying, which in-turn requires more precise and advanced evaluation approaches for assessing their microstructures and properties, such as a nanoindentation method. However, it is important to examine whether the required microstructure and phase information can be accurately obtained using the nanoindentation method. In this study, the hardness and Young's modulus were measured by the nanoindentation method and were statistically evaluated by the Weibull distribution. As a case study, alumina coatings deposited by atmospheric plasma spraying (APS) and high-velocity oxyfuel-flame spraying (HVOF) were examined. When medium-sized alpha-alumina powder was sprayed by APS, the coating consisted of alpha- and gamma-alumina, and the Weibull plot of the hardness showed a bimodal distribution. Conversely, in the case of small-sized powder sprayed by APS, the coating exhibited a gamma-phase and a unimodal distribution. When finer alpha-alumina powder was sprayed using HVOF, it consisted of alpha, gamma, and non-crystalline phases, and the Weibull plot revealed a bimodal distribution. The gamma and non-crystalline phases were considered to appear from molten states and as the alpha phase was believed to originate from the unmolten states of the particles. Therefore, the unimodal distribution was ascribed to the molten state of the particle, while the bimodal distribution to the molten and unmolten states. [doi:10.2320/matertrans.T-M2020866]

(Received September 29, 2020; Accepted November 30, 2020; Published January 25, 2021)

**Keywords:** ceramic coatings, plasma spray, HVOF, nanoindentation, Weibull distribution, alumina

## 1. Introduction

Recently, new coating-forming processes, such as thermal spraying using fine particles and the aerosol deposition (AD) method, have been reported for controlling the microstructure of ceramic spray coatings.<sup>1-7)</sup> In contrast to conventional ceramic spray coatings with pores and microcracks,<sup>8)</sup> the coatings obtained by these deposition processes have potential to become dense and nanostructured. As the importance of artificial intelligence (AI) and data science has been duly expounded, it is essential to create a database of the various physical properties of these thermal spray coatings, especially from the viewpoint of coating design.<sup>2,9,10)</sup> Since these spray coatings can have nanostructures, nanoscale-texture evaluation techniques, such as a nanoindentation method, are an important means to grasp the structure and mechanical properties of these coatings.<sup>11-13)</sup> For example, the nanoindentation method was used to investigate the properties of each nanostructure in the materials that consisted of multi-nanostructures.<sup>14,15)</sup>

When statistically evaluating properties of brittle materials, such as the hardness of a thermal spray coating, the Weibull distribution can more appropriately evaluate variations in mechanical properties than the Gaussian distribution.<sup>16)</sup> The Weibull plot exhibited a bimodal distribution due to the difference in properties between the nanostructure and the

molten structure derived from the granulated nano-particle powder in plasma spraying.<sup>17)</sup> Similar statistical methods have also been utilized to describe the bimodal distribution of yttria-stabilized zirconia (YSZ)<sup>18)</sup> and gray alumina,<sup>19)</sup> as well as to evaluate the uniformity of the mechanical properties of plasma-sprayed Al<sub>2</sub>O<sub>3</sub> coatings.<sup>13,20)</sup> Therefore, the Weibull distribution has been proven to be a useful statistical method for testing coatings having multiple phases.

However, the values obtained by the nanoindentation method could sometimes differ significantly from the macro-physical properties obtained by conventional test methods, such as the micro-Vickers measurement. Since those values of different thermal spraying processes have not been compared systematically, it was difficult to use the measured values for engineering purposes.<sup>21)</sup> Therefore, it is imperative that the methods of measuring the macro-mechanical properties of thermal spray coatings, such as Vickers and micro-Vickers measurements, are associated with the micro-mechanical property measurement methods, such as the nanoindentation technique. Herein, we utilize Al<sub>2</sub>O<sub>3</sub><sup>20,22-26)</sup> as a representative material of ceramics, and systematically measure the nanomechanical properties of various spray coatings by using the nanoindentation method. The range of application of the nanoindentation method to the representative scale of the coating microstructure was investigated. For alumina coatings deposited by atmospheric plasma spraying (APS) using two kinds of alumina powder with two different average particle sizes, we evaluated mechanical properties, such as hardness and Young's modulus, by the nanoindentation and micro-Vickers methods. For comparison, we also evaluated an alumina coating on which alumina powder with a finer particle size distribution was deposited

<sup>\*1</sup>This Paper was Originally Published in Japanese in J. Jpn. Therm. Spray Soc. **56** (2019) 154-161. The corrigendum was also published in Japanese in J. Jpn. Therm. Spray Soc. **57** (2020) 179. The content of the corrigendum has been reflected to this paper. The caption of Fig. 5 is slightly modified.

<sup>\*2</sup>Corresponding author, E-mail: kentaro.shinoda@aist.go.jp

Table 1 Spray conditions for APS.

Process	APS	
Powder (F&C) [ $\mu\text{m}$ ]	M (30-54)	S (5-25)
Torch	SG-100	
Substrate	SUS304	
Spray distance [mm]	90	60
Current [A]	900	
Voltage [V]	34	
Power [kW]	30.6	
Primary gas flow rate (Ar) [SLM* (SCFH**)]	24 (50)	
Secondary gas flow rate (He) [SLM (SCFH)]	24 (50)	

\* SLM denotes standard liter per minute.

\*\* SCFH denotes standard cubic feet per hour (1 SCFH = 0.47195 SLM).

Table 2 Spray conditions for HVOF.

Process	HVOF
Powder (F&C)	F (5-15)
Torch	JP-5000
Substrate	SUS304
Spray distance [mm]	150
Oxygen flow rate [SLM (SCFH)] / Pressure [kPa (PSI*)]	741 (1570) / 841 (122)
Kerosene flow rate [SLM (SCFH)] / Pressure [kPa (PSI)]	3.1 (6.5) / 834 (121)

\* PSI denotes pound-force per square inch (1 PSI = 6894.757 Pa).

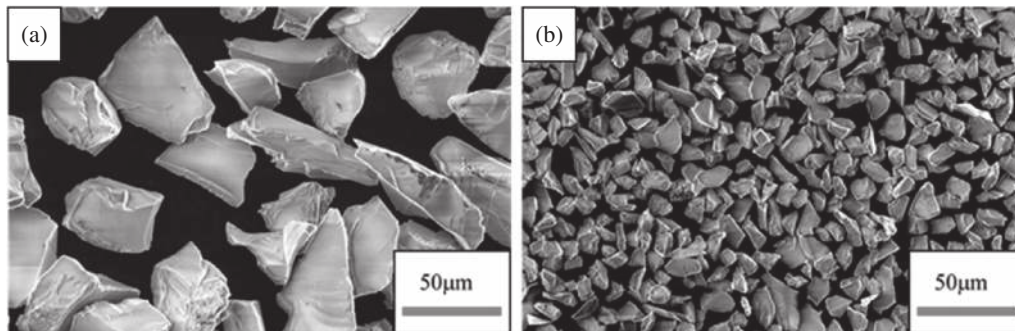


Fig. 1 SEM image of powder (a) Average particle size is 42  $\mu\text{m}$ , sieve particle size is 30–54  $\mu\text{m}$  (b) Average particle size is 15  $\mu\text{m}$ , sieve particle size is 5–25  $\mu\text{m}$ .

by high-velocity oxy-fuel (HVOF) flame spraying. The Weibull plot was utilized for statistical processing as alumina was generally brittle.

## 2. Experimental

### 2.1 Materials

The spraying conditions used in this experiment are listed in Tables 1 and 2 for the APS and HVOF, respectively. Figure 1 shows the scanning electron microscope (SEM) image of the powder used. Fused and crushed (F&C)  $\alpha\text{-Al}_2\text{O}_3$  powder manufactured by Fujimi Incorporated was used as the thermal spray material. SG-100 and JP-5000 torches

manufactured by TAFA/Praxair were used for APS and HVOF with the spray conditions presented in Tables 1 and 2, respectively. Stainless steel substrates (SUS 304, equivalent to AISI 304) were used as substrates. Two kinds of  $\alpha\text{-Al}_2\text{O}_3$  powder with two average particle sizes used in APS. By sieving, powder S with a particle size distribution of 5–25  $\mu\text{m}$  (average particle size of 15  $\mu\text{m}$ ) and powder M with particle sizes of 30–54  $\mu\text{m}$  (average particle size of 42  $\mu\text{m}$ ) were prepared; and the samples sprayed with them by APS were named APS-S and APS-M, respectively. For HVOF, the powder S was sieved and the powder F with 5–15  $\mu\text{m}$  (average particle size of 10  $\mu\text{m}$ ) was used, and the deposited sample was named HVOF-F.

Table 3 Indentation conditions.

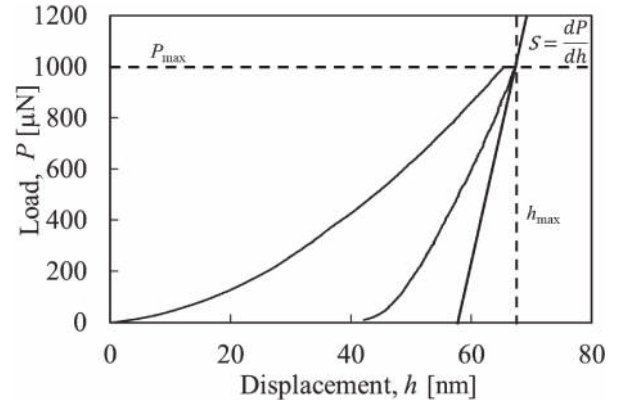
	Nanoindentation	Micro-Vickers
Working indenter	Berkovich	Vickers
Maximum load [mN]	1	100
Loading speed[mN/s]	0.2	13.3
Hold time [s]	2	5
Points	100	5

## 2.2 Phase identification of coating and observation of microstructure

X-ray diffraction (XRD) was used to identify the phase of the obtained coatings with a RINT-2000 X-ray diffractometer (Rigaku, Tokyo). Additionally, the cross section of the coatings was observed to study the microstructure. The coatings buried with a resin were cut by a fine cutter, followed by polishing starting from #200-SiC to 1  $\mu\text{m}$ -diamond buffing to have the cross section mirror-polished. Scanning electron microscope (SEM) (JSM-5500, JEOL Ltd., Tokyo) was used for the observation.

## 2.3 Nanoindentation test

The nanoindentation test was performed on the cross section of the sprayed coatings. Polishing of the cross section down to the surface roughness of 1  $\mu\text{m}$  was the same as that for the SEM. For further smoothness, the surface was additionally polished to 0.5  $\mu\text{m}$  using a diamond abrasive. After polishing, degreasing was performed using acetone and ethanol. Table 3 shows the test conditions in this experiment. The nanoindentation method, using TI Premier (Hysitron, Bruker Corp., MA, USA), was employed in evaluating the micro-mechanical properties of the spray coatings. This device had a scanning probe microscope (SPM) function and could measure the surface of the sample. Herein, this SPM function was used to observe the condition of the sample surface, and it was confirmed that there was no contamination at the test position. Measurement was also performed on a (0001) sapphire substrate (Furuuchi Chemical Co., Ltd./Tokyo), which can be regarded as a single crystal  $\alpha\text{-Al}_2\text{O}_3$  that represents a reference for the  $\alpha\text{-Al}_2\text{O}_3$  coating. For the testing machine, a standard sample of fused silica was tested under the same conditions as those for coatings to confirm the validity of the calibration. To separate the mechanical properties of each phase of the microstructure in the coating, which was observed by SEM, we attempted to reduce the indentation area by lowering the maximum load as much as possible. When the load was reduced, the curvature of the tip of the indenter could affect the determination of the area, and a deviation could occur between the area determined from the area function and the actual indentation area. Therefore, the lower load limit was determined to 1 mN so that the indented area could be measured. The hardness and Young's modulus were derived from the load-displacement curve obtained by the test using the method proposed by Oliver and Pharr, i.e., the O-P method.<sup>27)</sup> First, the area function of the indenter was determined using the results of testing a standard sample with multiple loads. Figure 2 shows

Fig. 2 Load ( $P$ )-Displacement ( $h$ ) curve.

the load-displacement curve obtained in this experiment. In the test, the projected area of the indentation at the maximum load was calculated from the eqs. (1) and (2):

$$h_c = h_{\max} - h_s = h_{\max} - \varepsilon \frac{P_{\max}}{S} \quad (1)$$

$$A(h_c) = 24.5h_c^2 + C_1h_c + C_2h_c^{1/2} + C_3h_c^{1/4} + \dots + C_5h_c^{1/16} \quad (2)$$

where  $h_s$  is the displacement of the sample surface,  $h_{\max}$  is the displacement at the maximum load, and  $\varepsilon$  is a constant depending on the shape of the indenter. Herein,  $\varepsilon = 0.75$  was used.  $P_{\max}$  is the maximum load,  $S$  is the contact stiffness, i.e., the slope of the tangent line at the highest point of the unloading curve from Fig. 2, and  $A$  is the projected area of the indentation. Equation (2) is a fabricated area function, and  $C_1$ – $C_5$  are constants determined from the load-displacement curve obtained from the fused silica test. The values used in this experiment were  $C_1 = -5639$ ,  $C_2 = 5.466 \times 10^5$ ,  $C_3 = -5.834 \times 10^6$ ,  $C_4 = 1.497 \times 10^7$ ,  $C_5 = -9.744 \times 10^6$ , and the indentation hardness was evaluated from the calculated projected area of the indentation. Hardness ( $H_{IT}$ ) and composite Young's modulus of samples were calculated from the following eqs. (3) and (4), respectively:

$$H_{IT} = P_{\max}/A(h_c) \quad (3)$$

$$E_{\text{eff}} = \frac{\sqrt{\pi}}{2\sqrt{A(h_c)}} \times S \quad (4)$$

Young's modulus calculated by the device was the  $E_{\text{eff}}$  of the sample and the indenter given by the expression in the following eq. (5):

$$\frac{1}{E_{\text{eff}}} = \frac{1 - \nu^2}{E} + \frac{1 - \nu_i^2}{E_i} \quad (5)$$

where,  $\nu$  is Poisson's ratio and the subscript  $i$  denotes those of the indenter. Since a diamond indenter was used in this experiment, 1140 GPa and 0.07 were used as Young's modulus and Poisson's ratio of the indenter, respectively. The median value of Poisson's ratio of  $\text{Al}_2\text{O}_3$ , i.e.,  $\nu = 0.24$ , was used.<sup>28)</sup>

Note that the hardness determined by nanoindentation could differ from that determined by a conventional method that utilized the size of the residual indentation when measuring the materials with large elastic recoveries during unloading, as well as materials with very high  $H_{\text{IT}}/E$  values. This difference could occur because the definition of the hardness in nanoindentation was based on the contact area between the indenter and the sample under loading.<sup>27,29)</sup>

The vicinity of the indentation tends to show a pile-up in case for metal materials when  $h_f/h_{\text{max}} > 0.7$  where  $h_f$  is the depth of the indentation after the test. The pile-up can cause the indentation periphery quite insignificant, resulting in the hardness and Young's modulus overestimated by the evaluation.<sup>30)</sup> Therefore, we tested several  $\text{Al}_2\text{O}_3$  coatings with different hardness values. When the hardness was 7.97 GPa,  $h_f/h_{\text{max}} = 0.66$ , and when the hardness was 27.7 GPa,  $h_f/h_{\text{max}} = 0.32$ ; thus, it was ascertained that  $h_f/h_{\text{max}} < 0.7$  over a wide range. Consequently, it was confirmed that the effect of the pile-up was quite negligible for the  $\text{Al}_2\text{O}_3$  coating as the object of this study.

Brittle material coatings were examined in this study. Thermal spray coatings were expected to have complex

microstructures due to the melting of the powder during the process; hence, a variation in results was expected. Therefore, the Weibull distribution was used for statistical analysis of the data.<sup>16,17,19)</sup>

DUH-211 (Shimadzu Corporation, Kyoto) was used for the micro-Vickers test. The ISO standard does not recommend a comparison between Vickers hardness and nanoindentation hardness.<sup>31)</sup> However, when the hardness is standardized in the same unit and derived with the same method, the relationship between the projected area and depth has been demonstrated to be self-similar.<sup>32,33)</sup> In this experiment, the Vickers hardness (HV) value was obtained from the hardness derivation formula using the following relation to divide the load by the projected area to compare the coating hardness with the conventional method. Equation (6) converts the unit to GPa and sets it as  $H_{\text{micro}}$ .<sup>33)</sup>

$$H_{\text{micro}} = \frac{HV \times 9.8}{1000 \times \sin 68^\circ} \quad (6)$$

By using  $H_{\text{micro}}$ , we examined the degree of deviation of the hardness of the coating in the nanoindentation test conducted herein from the widely used Vickers hardness.

### 3. Experimental Results

#### 3.1 Results of microstructure observation

Figure 3 shows the results of SEM observation for the cross section of the coatings. Figures 3(a) and (b), reveal that in APS-M, in addition to the lamellar structure consisting of splat layers typically found in thermally sprayed coatings, spherical particle structure approximately  $20 \mu\text{m}$  was

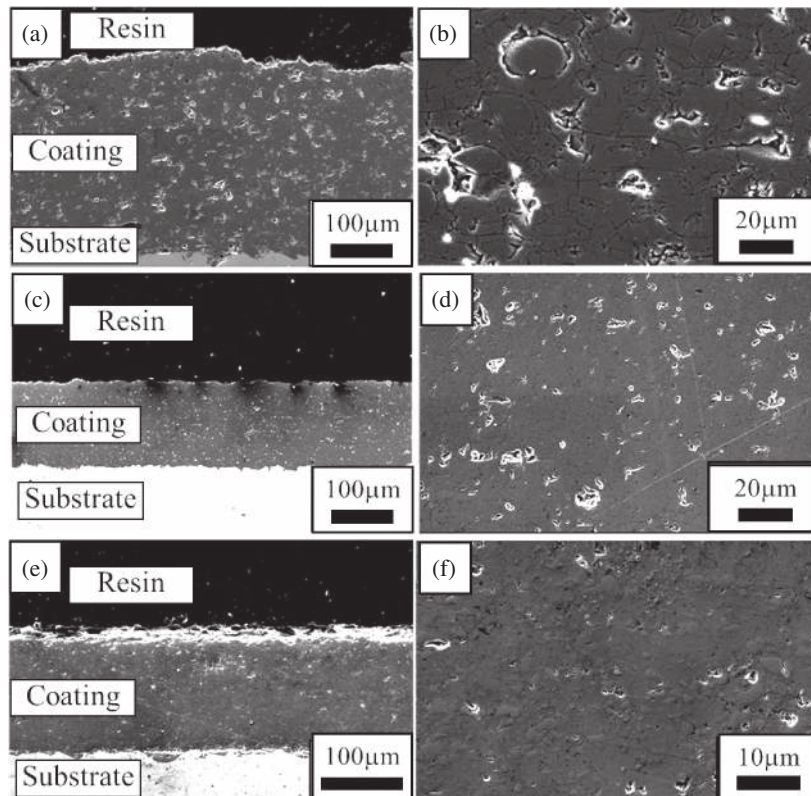


Fig. 3 Cross-sectional SEM images (a) APS-M ( $30\text{--}54 \mu\text{m}$ ) low magnification, (b) APS-M high magnification, (c) APS-S ( $5\text{--}25 \mu\text{m}$ ) low magnification, (d) APS-S high magnification, (e) HVOF-F ( $5\text{--}15 \mu\text{m}$ ) low magnification, (f) HVOF-F high magnification.



observed on the cross section of the coating, suggesting that unmolten particles were trapped in the coating in addition to flattened splats built from impaction of fully molten particles. Furthermore, large pores approximately  $20\text{ }\mu\text{m}$  were observed. On the contrary, in Figs. 3(c) and (d), the observed microstructure was very different from those of Figs. 3(a) and (b); that is, the pore size was below  $10\text{ }\mu\text{m}$  and the microstructure suggested that powder particles were melted well in APS-S despite of the same APS process.

Figures 3(e) and (f) indicate that the HVOF-F coating had a further small pore size than the APS coating, and the pore size in the coating observable from Fig. 3(f) was below  $10\text{ }\mu\text{m}$ . At a higher magnification, a spherical structure similar to APS-M was observed in the coating, but the diameter was approximately  $2\text{ }\mu\text{m}$ . This is also assumed to be due to the entrainment of unmolten or partially unmolten particles.

Figure 4 presents the results of the XRD phase identification for each of the APS and HVOF coatings. The  $\text{Al}_2\text{O}_3$  coatings obtained by APS shows a difference in the coating microstructure depending on the particle size of the starting material. The composition of this APS-S was confirmed to be near-totally consisting of  $\gamma\text{-Al}_2\text{O}_3$ , which was a metastable phase, and  $\alpha\text{-Al}_2\text{O}_3$  derived from the raw material powder was almost absent. On the contrary, in APS-M, the peak intensity of  $\alpha\text{-Al}_2\text{O}_3$  was higher than that of APS-S, and it was confirmed that both  $\gamma\text{-Al}_2\text{O}_3$  and  $\alpha\text{-Al}_2\text{O}_3$  were included. In the diffraction pattern of HVOF-F, in addition to the peaks of  $\gamma\text{-Al}_2\text{O}_3$  and  $\alpha\text{-Al}_2\text{O}_3$ , a very broad peak was observed on the low angle side. This suggests that in the HVOF coating deposited under these conditions, an amorphous phase existed in addition to the crystalline phase.

### 3.2 Nanoindentation test results

Figure 5 shows the relationship between the hardness and Young's modulus obtained by the nanoindentation and

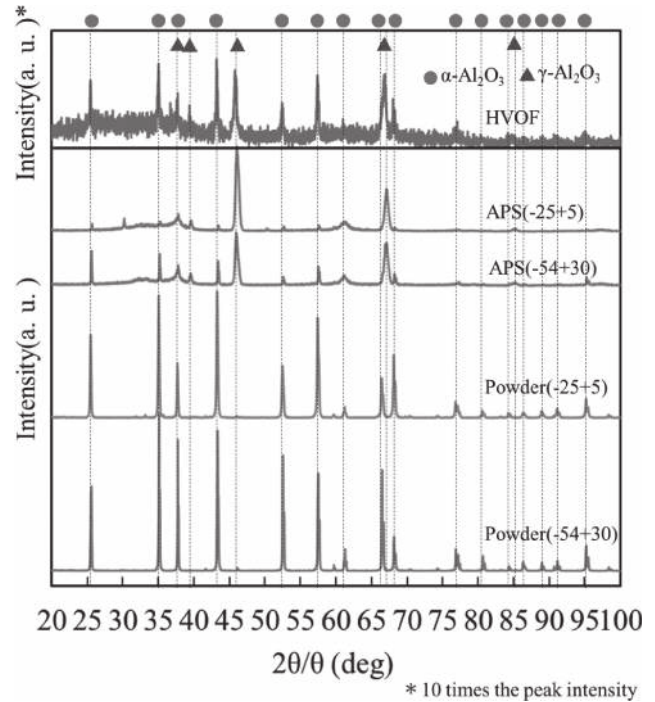


Fig. 4 Powder and coating XRD patterns.

micro-Vickers methods. Single crystal sapphire as a reference showed a hardness in the vicinity of 27 GPa and sometimes also showed a measured value of 36 GPa. In some cases, a 1 mN load left insufficient indentation, leading to a higher hardness value. In such a case, an additional test was performed at a load of 10 mN, revealing the hardness of  $26.5 \pm 0.6\text{ GPa}$ , which was consistent with the measured value of 27 GPa at 1 mN. These results indicate that a 1 mN load was the lower limit when measuring the single crystal sapphire, which represents the reference of high hardness side; thereby suggesting that the hardness measurement of APS and HVOF coatings were conducted without problems.

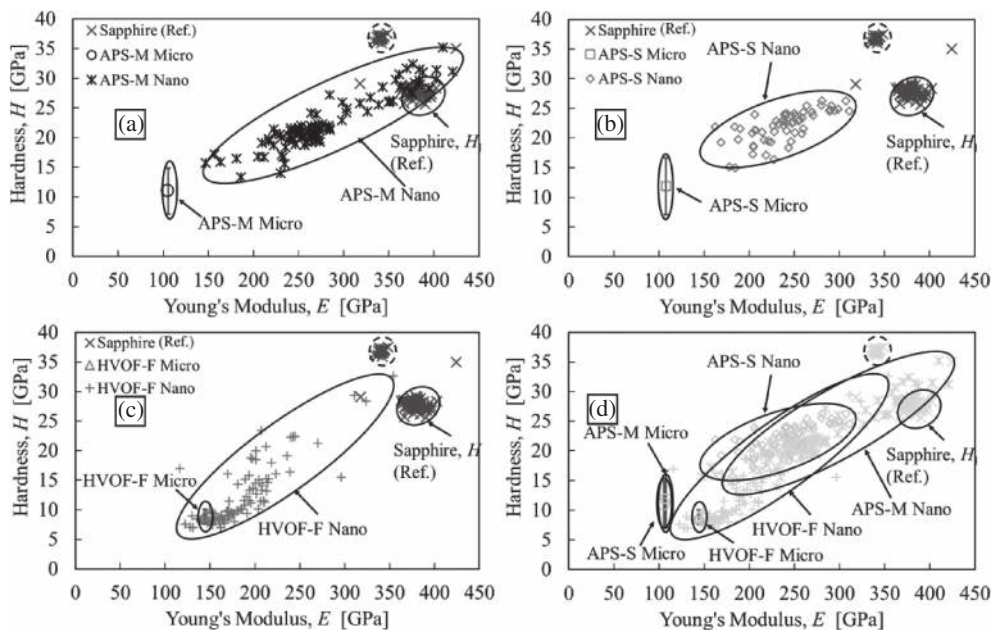


Fig. 5 Modulus vs. hardness in thermally sprayed alumina coatings.

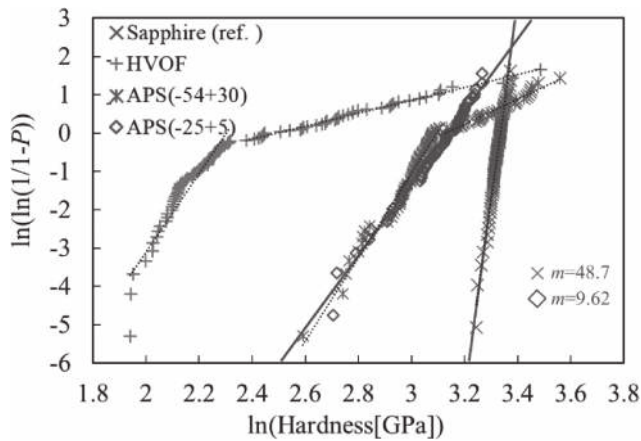


Fig. 6 Weibull distribution of the hardness of the thermally sprayed alumina coatings.

Figure 5(d) depicts that there was a positive correlation between the hardness and Young's modulus in the results of the nanoindentation test. The nanoindentation hardness of APS coatings generally tended to be higher than that of HVOF, as compared in Figs. 5(a) to 5(d). Furthermore, Figs. 5(a) to (c) show that the value of the micro-Vickers hardness was significantly different from that of nanoindentation hardness in the APS coating. The hardness value differed by 5 GPa and Young's modulus by 50 GPa. Meanwhile, the value of HVOF coatings was close the lower limit of nanoindentation.

Figure 6 shows the results of the properties of the thermal spray coatings arranged by the Weibull plots. The hardness of APS-M and HVOF-F exhibited a bimodal distribution having two slopes. On the contrary, the APS-S and reference sapphire substrates had a single distribution. Notably, the area of the lower hardness of APS-M was almost overlapped with that of the hardness distribution of APS-S. The bimodal distribution of the HVOF-F coating showed that the maximum hardness of the HVOF-F coating reached nearly that of the APS coating, while the minimum hardness, approximately 7–10 GPa, was significantly lower than that of APS coating.

Figure 7 displays the SPM image obtained using a nanoindenter for the sample exhibiting a bimodal distribution. The SPM images of both coatings revealed circular-shaped objects, as shown in region a, of which surfaces were 170 nm and 50 nm higher than the surroundings at APS-M and HVOF-F, respectively. Note that these surface asperities were flat enough compared to the surface smoothness of the coatings obtained by mirror polishing with a 0.5  $\mu\text{m}$  abrasive. The rest flat part was named region b. Table 4 shows the hardness values measured in each region a and b in Fig. 7. Both coatings showed a hardness of 27 GPa or more in region a, while the hardness of each coating was different

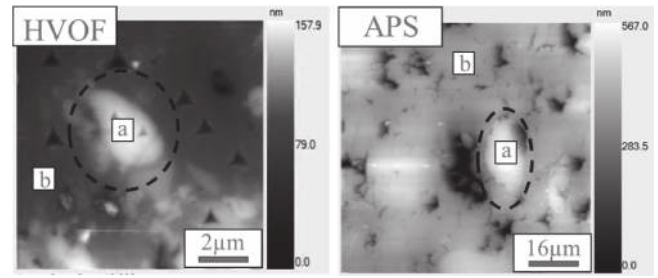


Fig. 7 SPM images of coatings with a bimodal distribution. The SPM image shows that the higher the brightness, the higher the surface compared to the surrounding area.

in region b; and the coating of APS-M and HVOF-F had a hardness value of approximately 18 GPa and 11 GPa, respectively.

#### 4. Discussion

This experiment revealed a positive correlation between hardness and Young's modulus, yet it has often been mentioned that hardness and Young's modulus were inherent indicators of plastic and elastic deformation, respectively, and discussion on the correlation between the two factors was rare. This correlation has been previously investigated in the field of cemented carbide materials.<sup>34,35</sup> Here, a test was conducted between two phases in a composite coating, and the characteristics of such a composite coating revealed to be expressed by the mixing rule of each coating. Therefore, we consider that the existence of a correlation is appropriate to some extent herein.

In the Weibull plot, it was confirmed that the small-diameter APS coating with an average particle size of approximately 15  $\mu\text{m}$  had a unimodal distribution, while that with a mean particle size of 42  $\mu\text{m}$ , as well as the HVOF coating had a distribution that could be regarded as bimodal. The bimodal distribution under certain conditions suggests that there are situations wherein the coating structure consists of multiple phases rather than a single one, depending on the thermal spray conditions.<sup>17</sup> Here, we would like to classify the coating microstructure from the viewpoint of coating formation process.

First, molten state of the particles at impact is important. In this study, we sprayed the coatings under the recommended spraying conditions of the powder manufacturer. Herein, we would like to discuss the state of the in-flight particles.

In-flight status of the F&C alumina powder with a particle size of 10–45  $\mu\text{m}$  measured by an in-flight particle monitoring system, Accuraspray (Tecnar, Quebec, Canada) under the same plasma spray conditions.<sup>36</sup> At the spray distances of the 60 mm, 90 mm, and 120 mm, the average velocities of the in-flight particles were 341 m/s, 322 m/s, and 294 m/s, respectively, and the average surface temper-

Table 4 The hardness comparison of (a) circular area in SPM image and (b) other flat area in SPM image in Fig. 7.

	APS-M	HVOF-F
a	27.8 GPa	27.4 GPa
b	18.0 GPa	10.7 GPa

atures were 2809°C, 2723°C, and 2656°C, respectively. Although the purity of this powder was higher than that used in this study, there was no difference in powder shape and apparent density. When the F&C powder with particle sizes of 5–25 µm was measured at 90 mm under the same conditions, the average velocity of in-flight particles was 342 m/s and the average surface temperature was 3054°C. Based on this information, the particle state under the present experimental conditions was estimated below. The average particle size of 30–54 µm particles was larger than that of the 10–45 µm particles. At the 90 mm position, it was assumed that the average velocity was lower than 322 m/s, and the average surface temperature was below 2723°C. Nonetheless, it was predicted that the average velocity exceeded 342 m/s, and the average surface temperature was above 3054°C under the conditions of APS-S and at a deposition distance of 60 mm. For HVOF,<sup>36)</sup> on measuring a 10–45 µm powder of WC–10Co–4Cr, which was a different material from this study, at the positions of 330 mm, 380 mm, and 430 mm from the torch outlet under the same spraying input conditions, the average velocities were 1002 m/s, 815 m/s, and 697 m/s, while the average surface temperatures were 1923°C, 1744°C, and 1672°C, respectively. In case of finer particles 5–30 µm in diameter at the position of 380 mm, the average velocity and average surface temperature were 861 m/s and 1895°C, respectively. Considering that the spray distance was 150 mm and the particle size was much smaller in this study, and that the specific gravity of alumina is much lower than for WC–10Co–4Cr, the particle velocity in this study was expected to exceed 1002 m/s.

Zhang *et al.* proposed a concept referred to as the melting index (MI) as an indicator of the melting state of particles.<sup>37–39)</sup> Since there is a temperature gradient in actual particle heating, the surface temperature of the particles measured by in-flight particle sensors does not necessarily represent the molten state of the particles. Therefore, MI was created as an index to study the molten state of particles. This effect is remarkable especially for ceramic materials with low thermal conductivities. Simply put, the longer the residence time of a particle in a heat source, such as a plasma or combustion flame, the more the inside will melt, even at the same surface temperature. Since particles were internally supplied at the torches used herein in the APS and HVOF, it was difficult to perform simple calculations based on simple assumptions described in the reference. Yet, dimensional analysis suggested that the time required for the particles to melt was shown to be inversely proportional to the square of the particle diameter. Therefore, for APS, the time required for melting of APS-S is shortened to 1/9 compared to that of APS-M because the average particle size of APS-S is approximately 1/3 of that of APS-M. Meanwhile, the measurement results suggested the velocity of APS-S would not be twice as high as that of APS-M. Therefore, considering that the spray distance was 2/3 of that of APS-M, the residence time of APS-S is only shortened to approximately 1/3 of APS-M. Thus, by decreasing the particle size, the residence time is shortened, while the time required for melting is further reduced, indicating that the particles are better melted. For HVOF, although a gas-fuel

type with a high combustion temperature was partly used for alumina spraying,<sup>26,40)</sup> a liquid-fuel type, such as JP-5000, having a low flame temperature was merely used for spraying high-melting-point ceramic materials such as alumina. However, considering that the 10–45 µm WC–10Co–4Cr powder was heated to 1923°C, and considering that the melting point of alumina is 2072°C, while the flame temperature can reach 2120°C,<sup>41)</sup> smaller particles in 5–15 µm particles can also reach the melting point of alumina based on the previous discussion on particle sizes. As the average particle size is 10 µm, the small particles in the distribution are approximately 1/4 to 1/8 in size, thus, it is reasonable to think that some of the particles are melted. Therefore, for the HVOF herein, it is concluded that some particles may have melted and collided, and the speed was considered to be very high ( $\geq 1000$  m/s).

The results of XRD showed that the coatings deposited by APS had different compositions depending on the starting powder size. During the spray coating process, the particle size and residence time were related to the melting of the sprayed powder in APS.<sup>42)</sup> Since the raw material powder used herein was  $\alpha$ -Al<sub>2</sub>O<sub>3</sub>, the  $\alpha$  phase observed in the coating was considered to be attributed to unmolten particles. Meanwhile, the  $\gamma$ -Al<sub>2</sub>O<sub>3</sub>, which is a metastable phase, observed in the coating was originated from molten particles. Generally, HVOF has particles impacting on the substrate at higher velocity than APS; hence, the particle cooling rate is faster than APS, which can result in the formation of an amorphous phase in the first layer of the Al<sub>2</sub>O<sub>3</sub> coating.<sup>25)</sup> However, the HVOF coating in this experiment produced an amorphous phase within the coating, which differs from what previous literature reports. The purity of the Al<sub>2</sub>O<sub>3</sub> powder used for coating formation herein was 99%, therefore, it is unlikely that the coating became amorphous due to impurities. Thus far, most of the HVOF-sprayed alumina coatings were of the gas fuel type. For the HVOF of high-speed and low-temperature liquid fuel types, such as JP-5000, the amorphous phase may more likely appear than usual. Other associated factors may include the presence of water vapor during thermal spraying. We would like to pursue their identification in the near future as it is beyond the scope of this study.

Thus, it is natural to think that the bimodal distribution in the Weibull plot of the hardness of the sprayed coating corresponds to the presence of the molten and unmolten phases in the coating. The hardness and Young's modulus in the indentation test are known to be sensitive to the crystal structure. In case of Al<sub>2</sub>O<sub>3</sub>, the hardness is known to be higher in the order of  $\alpha$ -Al<sub>2</sub>O<sub>3</sub>,  $\gamma$ -Al<sub>2</sub>O<sub>3</sub>, and the amorphous phase.<sup>43)</sup> In this experiment,  $\alpha$ -Al<sub>2</sub>O<sub>3</sub>, which is an unmolten phase in both APS-M and HVOF-F coatings, is considered to correspond to the higher hardness distribution in the Weibull distribution.

The microstructure of the melt phase differs considerably among processes. Regarding the hardness of the melt phase in APS-M, the distribution on the lower hardness side in the Weibull distribution was between 13.3 GPa and 22.3 GPa. However, in HVOF, it was between 7.0 and 10.1 GPa, suggesting that the hardness of the melt phase was greatly reduced in HVOF. A non-negligible amount of amorphous



phase in the HVOF melt phase thereby reduced the microhardness of the melt phase.

Lima *et al.* conducted a Knoop hardness test on YSZ-sprayed coatings with nanostructures.<sup>17)</sup> Although the Weibull distribution showed bimodal results, the higher hardness phase was originated from the molten phase. In other YSZ results, Lamata *et al.* also reported a bimodal distribution in YSZ coatings, which suggested that the hardness of the molten phase was higher than in the partially melted region.<sup>18)</sup> Conversely, Wang *et al.* also conducted a nanoindentation test and Vickers hardness test on nanostructured YSZ, but the results showed that the unmolten-phase region had a high hardness, which indicates a different tendency compared to other studies.<sup>44)</sup> In our study, we used sintered  $\text{Al}_2\text{O}_3$  powder as raw materials, not nanostructured YSZ. Therefore, the unmolten region was not a nanostructure, but remained a sintered region of the initial raw material particles having higher hardness. We also conducted indentation at a lower load, so the measured region was minimal. Thus, it can be inferred that the properties of the corresponding microstructure was more close to that of single crystal.

Wang *et al.* investigated the relationship between the plasma spray parameters and the microstructure of gray alumina by using a microhardness.<sup>19)</sup> The hardness results also showed a bimodal distribution, but the average hardness was approximately 18 GPa at most and the highest hardness was approximately 20 GPa in the Weibull distribution, which were lower than this study. They used agglomerated powder, which differs from our study. Additionally, since their test load was 1.96 N, which massively differs herein, the size of the indentation varies due to the different loading, resulting in the fluctuation of the ratio of the defects in the indentation and subsequently the fluctuation of the indentation properties.

The Weibull distribution has been used as an index of uniformity for APS coatings,<sup>7,20)</sup> but herein, it is shown that it is an effective means for high-speed and low-temperature particle processes, such as HVOF coatings. This entails that the Weibull distribution is also effective for comparison between spraying processes.

It has been reported that the mechanical properties of an entire coating can be predicted by applying the rule of mixture to the mechanical properties of its constituent phases.<sup>17,44)</sup> However, before going to consider the rule of mixture, we need to consider the difference between the micro-Vickers hardness and the nanoindentation hardness in this study. As shown in the cross-section of the coating in Fig. 3, thermal spray coatings have many defects such as cracks and pores, which decrease actual coating properties. In the micro-Vickers test, the larger indentation area easily involves such defects. Therefore, it is currently difficult to match the results of the nanoindentation test to those of the micro-Vickers test. However, if such a divergence is attributed to these defects, it conversely implies that we can match these results when ceramic coatings having a finer structure without defects are examined. Determination of such a threshold value of the defect size and frequency will be important in the future.

Regarding the hardness of each phase of  $\text{Al}_2\text{O}_3$ , which was deposited by sputtering though, Engelhart *et al.* reported

that the hardness of the amorphous phase decreased to approximately half of that of  $\gamma\text{-Al}_2\text{O}_3$ .<sup>43)</sup> HVOF-F melt phase hardness was approximately half of that of the APS-M melt phase ( $\gamma$  phase). Therefore, it is considered that the amorphous phase also exists in our study.

Regarding the structures of the molten and unmolten phases of APS-M and HVOF-F, Figs. 3 and 7, as well as Table 4 confirmed the presence of the molten phase around the circular unmolten phase. However, we could not obtain information on how the amorphous and  $\gamma\text{-Al}_2\text{O}_3$  phases were coexisted in the molten phase in HVOF. In order to measure individual mechanical properties of each domain in the coating by the nanoindentation test, it is necessary to use the indenter smaller than the mixed domain size.<sup>14)</sup> Our result indicates that the molten phase in HVOF has a fine structure because of rapid quenching, and therefore it still poses challenges to quantify the coating structure by the current nanoindentation technique.

## 5. Conclusion

Nanoindentation tests were performed on thermally sprayed alumina coatings deposited by APS and HVOF, and the following conclusions were obtained through the comparison between the processes.

- (1) There was a positive correlation between the hardness and Young's modulus of the coating at the nano-indentation test. In any case, there was a discrepancy between the nanoindentation test and the micro-Vickers test. This discrepancy was attributed to defects, such as fine pores and cracks in the coating.
- (2) The Weibull distribution of the hardness exhibited a bimodal distribution at APS using large particles and HVOF. The bimodal distribution was attributed to the hardness difference of the molten and unmolten phases.
- (3) The HVOF coating is considered to have  $\gamma\text{-Al}_2\text{O}_3$  and amorphous phase in the molten phase, but it was difficult to separate the hardness of each phase. This is probably because the  $\gamma\text{-Al}_2\text{O}_3$  and amorphous phase coexist in the molten phase at a mixed state and the indentation size is not small enough to distinguish them.

## REFERENCES

- 1) J. Akedo and K. Shinoda: Thermal Spraying Technique **37**(3) (2018) 93–97 (in Japanese).
- 2) K. Shinoda, H. Noda, K. Ohtomi, T. Yamada and J. Akedo: *Int. J. Automat. Technol.* **13** (2019) 419–431.
- 3) H. Saito, T. Suzuki, T. Fujino and M. Suzuki: *J. Jpn. Therm. Spray Soc.* **54** (2017) 48–54 (in Japanese).
- 4) H. Saito, T. Suzuki, T. Fujino and M. Suzuki: *Mater. Trans.* **59** (2018) 1791–1797.
- 5) R. Yanaoka, Y. Ichikawa, K. Ogawa, T. Masuda and K. Sato: *J. Jpn. Therm. Spray Soc.* **56** (2019) 2–7 (in Japanese).
- 6) A. Vardelle *et al.*: *J. Therm. Spray Technol.* **25** (2016) 1376–1440.
- 7) D. Kindole, I. Anyadiegwu, Y. Ando, Y. Noda, H. Nishiyama, S. Uehara, T. Nakajima, O.P. Solonenko, A.V. Smirnov and A.A. Golovin: *Mater. Trans.* **59** (2018) 462–468.
- 8) Y. Yamazaki, T. Nishi and A. Ota: *J. Jpn. Therm. Spray Soc.* **53** (2016) 136–141 (in Japanese).
- 9) Y. Yamazaki and S. Izutsu: *J. Jpn. Therm. Spray Soc.* **56** (2019) 49–56 (in Japanese).
- 10) T. Kuwashima, Y. Morita and H. Waki: *J. Jpn. Therm. Spray Soc.* **56**



- (2019) 107–113 (in Japanese).
- 11) T. Ohmura and K. Tsuzaki: *Materia Japan* **46** (2007) 251–258 (in Japanese).
  - 12) S. Saber-Samandari and K.A. Gross: *Surf. Coat. Technol.* **203** (2009) 3516–3520.
  - 13) B. Dhakar, S. Chatterjee and K. Sabiruddin: *Mater. Sci. Technol.* **33** (2017) 285–293.
  - 14) G. Constantinides, K.S. Ravi Chandran, F.J. Ulm and K.J. Van Vliet: *Mater. Sci. Eng. A* **430** (2006) 189–202.
  - 15) N. Song, Z. Wang, Y. Xing, M. Zhang, P. Wu, F. Qian, J. Feng, L. Qi, C. Wan and W. Pan: *Materials* **12** (2019) 1677.
  - 16) C.K. Lin and C.C. Berndt: *J. Mater. Sci.* **30** (1995) 111–117.
  - 17) R.S. Lima, A. Kucuk and C.C. Berndt: *Mater. Sci. Eng. A* **327** (2002) 224–232.
  - 18) C. Lamuta, G. Di Girolamo and L. Pagnotta: *Ceram. Int.* **41** (2015) 8904–8914.
  - 19) H.-D. Wang, J.-L. Ma, G.-L. Li, J.-J. Kang and B.-S. Xu: *Appl. Surf. Sci.* **314** (2014) 468–475.
  - 20) Y. An, S. Li, G. Hou, X. Zhao, H. Zhou and J. Chen: *Ceram. Int.* **43** (2017) 5319–5328.
  - 21) L. Qian, M. Li, Z. Zhou, H. Yang and X. Shi: *Surf. Coat. Technol.* **195** (2005) 264–271.
  - 22) T. Shinohara, M. Adachi, Y. Takatani and Y. Harada: *J. Jpn. Therm. Spray Soc.* **53** (2016) 55–60 (in Japanese).
  - 23) R. McPherson: *J. Mater. Sci.* **15** (1980) 3141–3149.
  - 24) R. Musalek, J. Matejcek, M. Vilemova and O. Kovarik: *J. Therm. Spray Technol.* **19** (2010) 422–428.
  - 25) L. Li, B. Kharas, H. Zhang and S. Sampath: *Mater. Sci. Eng. A* **456** (2007) 35–42.
  - 26) M. Oksa, E. Turunen, T. Suhonen, T. Varis and S.-P. Hannula: *Coatings* **1** (2011) 17–52.
  - 27) W.C. Oliver and G.M. Pharr: *J. Mater. Res.* **7** (1992) 1564–1583.
  - 28) CES Selector, (Granta Design, 2018).
  - 29) W.C. Oliver and G.M. Pharr: *J. Mater. Res.* **19** (2004) 3–20.
  - 30) A. Bolshakov and G.M. Pharr: *J. Mater. Res.* **13** (1998) 1049–1058.
  - 31) K. Hattori, K. Miyahara and S. Yamamoto: *J. Mater. Test. Res. Assoc. Jpn.* **49** (2004) 223–234 (in Japanese).
  - 32) A.E. Giannakopoulos, P.L. Larsson and R. Vestergaard: *Int. J. Solids Struct.* **31** (1994) 2679–2708.
  - 33) D. Goldbaum, J. Ajaja, R.R. Chromik, W. Wong, S. Yue, E. Irissou and J.-G. Legoux: *Mater. Sci. Eng. A* **530** (2011) 253–265.
  - 34) J. Haines, J.M. Léger and G. Bocquillon: *Annu. Rev. Mater. Res.* **31** (2001) 1–23.
  - 35) X. Jiang, J. Zhao and X. Jiang: *Comput. Mater. Sci.* **50** (2011) 2287–2290.
  - 36) K. Sato: *Private Communication*, (2016).
  - 37) S. Sampath, V. Srinivasan, A. Valarezo, A. Vaidya and T. Streibl: *J. Therm. Spray Technol.* **18** (2009) 243–255.
  - 38) W. Zhang and S. Sampath: *J. Therm. Spray Technol.* **18** (2009) 23–34.
  - 39) H. Zhang, H. Xiong, L. Zheng, A. Vaidya, L. Li and S. Sampath: *ASME 2002 Inter. Mech. Eng. Cong. Expo.*, (2002) pp. 309–316.
  - 40) E. Turunen, T. Varis, S.-P. Hannula, A. Vaidya, A. Kulkarni, J. Gutleber, S. Sampath and H. Herman: *Mater. Sci. Eng. A* **415** (2006) 1–11.
  - 41) H. Tabbara and S. Gu: *Surf. Coat. Technol.* **204** (2009) 676–684.
  - 42) H.-B. Xiong and L.-L. Zheng: *Int. J. Heat Mass Transfer* **48** (2005) 5121–5133.
  - 43) W. Engelhart, W. Dreher, O. Eibl and V. Schier: *Acta Mater.* **59** (2011) 7757–7767.
  - 44) L. Wang, Y. Wang, X.G. Sun, J.Q. He, Z.Y. Pan and C.H. Wang: *Vacuum* **86** (2012) 1174–1185.